

# Carrier escape mechanism dependence on barrier thickness and temperature in InGaN quantum well solar cells

J. R. Lang,<sup>1</sup> N. G. Young,<sup>1</sup> R. M. Farrell,<sup>1</sup> Y.-R. Wu,<sup>2</sup> and J. S. Speck<sup>1</sup>

<sup>1</sup>*Department of Materials, University of California, Santa Barbara, California 93106, USA*

<sup>2</sup>*Department of Electrical Engineering, Graduate Institute of Photonics and Optoelectronics, National Taiwan University, Taipei 10617, Taiwan*

(Received 23 May 2012; accepted 17 October 2012; published online 29 October 2012)

The properties of quantum well carrier escape were studied by varying barrier thicknesses in InGaN/GaN multi-quantum well solar cell devices. The dependence of the photocurrent on applied bias and temperature exhibited properties indicative of the quantum well carrier escape mechanisms of thermionic emission and tunneling, with tunneling dominating for thin barriers and high fields. Simulations using a self-consistent drift-diffusion and Schrödinger solver with analytical formulas extracted carrier escape lifetimes. By employing sufficiently thin barriers, it was found that escape lifetimes can be made small compared to recombination lifetimes, leading to high internal quantum efficiency. © 2012 American Institute of Physics. [<http://dx.doi.org/10.1063/1.4765068>]

To increase the efficiency and power density of concentrated photovoltaic (CPV) power systems, it is necessary to increase the number of junctions in a multijunction cell and to increase the bandgap energy of the top cell above 2 eV,<sup>1</sup> with an ideal of 2.5–2.6 eV for a 5 junction bonded hybrid cell.<sup>2,3</sup> A candidate material for the top junction is InGaN, which is already highly developed for light emitting diodes (LEDs). Recent progress in the development of InGaN-based photovoltaic technology has demonstrated clear performance advantages for multi-quantum well (MQW) devices<sup>4,5</sup> as opposed to quasi-bulk p-i-n double heterostructure devices.<sup>6,7</sup> To advance the development of InGaN photovoltaic technology, it is important to understand the dominant operational device physics. Details of charge carrier transport in these devices, beginning with the escape of photogenerated carriers from quantum wells (QWs), have, however, received relatively little attention. As the direction of InGaN-based PV research has moved to LED-like structures, additional insight for emitter devices can be gained from detailed study of microscopic processes in MQW solar cells.

It has already been established that internal polarization fields have a strong effect on carrier collection in drift-based InGaN solar cells,<sup>8,9</sup> which can be mitigated by high n-side doping.<sup>10</sup> Some of the spectral effects of varying internal fields through barrier thickness in InGaN MQW solar cell devices have also been explored previously.<sup>11</sup> By holding InGaN composition constant, the field-induced absorption edge red-shift for structures with thicker barriers is apparent, as the electron/hole bound states corresponding to the fundamental interband optical transition sit at lower energies with larger well fields. The absorption edge broadening seen accompanying this quantum confined stark effect (QCSE)<sup>12</sup> red-shift has been a challenge for MQW InGaN solar cells because of the gradual quantum efficiency roll-off near the absorption edge (see Refs. 4 and 5). In addition to the observation of field dependent spectral effects, this work establishes a barrier thickness-dependent transition of carrier transport from tunneling dominated at low barrier thickness and high field to thermionic emission dominated at high bar-

rier thickness and low field by varying temperature and bias during photocurrent measurements of InGaN MQW solar cell devices.

All samples were grown on 3.5  $\mu\text{m}$  thick conductive MOCVD-grown GaN:Si templates on sapphire by Lumilog with Si-doping concentration nominally  $2 \times 10^{18} \text{ cm}^{-3}$  and threading dislocation density of  $\sim 5 \times 10^8 \text{ cm}^{-2}$ . Growth was performed using  $\text{NH}_3$ -based molecular beam epitaxy (MBE), which has demonstrated very low leakage vertical devices<sup>13</sup> and activated as-grown p-type material.<sup>14</sup> First, a two-step highly doped GaN:Si buffer layer of 20 nm thickness was grown with  $[\text{Si}] \sim 4 \times 10^{18} \text{ cm}^{-3}$  followed by another 20 nm with  $[\text{Si}] \sim 1 \times 10^{19} \text{ cm}^{-3}$  (see Ref. 10). Then, 2.5 nm UID InGaN QWs with a composition of  $\text{In}_{0.11}\text{Ga}_{0.89}\text{N}$  were grown, followed by a QW growth temperature GaN capping layer 2 nm in thickness, a growth interrupt, and rapid heating to grow a high temperature GaN barrier layer. This modulated growth was repeated for a total of 15 quantum well/barrier pairs. Finally, a p-type layer was grown with  $[\text{Mg}] \sim 5 \times 10^{19} \text{ cm}^{-3}$  and a thickness of 150 nm (see Ref. 15 for growth details).

Three samples were grown holding all variables but the GaN barrier layer thickness constant. Samples A, B, and C had 3.8, 6.5, and 9.7 nm total GaN barrier (cap layer and high-temperature barrier) thicknesses per period, respectively. Impurity concentrations were measured via secondary ion mass spectroscopy (SIMS) measurements performed at Evans Analytical Group on calibration samples grown in identical conditions in our reactor. Intentional doping was calibrated by Hall-effect and SIMS, while layer thicknesses were calibrated by high-resolution x-ray diffraction, as in our previous work.<sup>16</sup> Atomic force microscopy (AFM) was used to confirm a smooth ( $<0.5 \text{ nm}$  RMS roughness for a  $5 \times 5 \mu\text{m}$  scan) top p-GaN surface. Device processing (see Ref. 16) resulted in square mesa isolated devices with a mesa edge length of 0.5 mm and top mesa grid contact fingers of 5  $\mu\text{m}$  width and 0.1 mm spacing.

Room temperature device testing was performed using procedures outlined in Ref. 16 with an unfiltered 300 W Xe

arc lamp (Oriel model 6258) at  $\sim 1$  sun intensity and monochromator for broadband illumination and spectrally resolved measurements, respectively. External quantum efficiency (EQE) was measured using a calibrated Si photodetector to measure input photon flux during monochromatic illumination. No optical enhancements were applied to the samples, and testing was performed on a black absorber to suppress multi-pass illumination. Elevated temperature measurements were performed by integrating a thermoelectric heater into the solar simulator system, with temperature data from a thermocouple in contact with the device side of the sample. Low temperature measurements were performed on a cryogenic vacuum probe station for which we report the stage temperature. The light source used for the low temperature measurements was a 100 W Hg arc lamp (Omnicure S1000). The light intensity with this source was approximately calibrated by matching the short-circuit photocurrent of the measured devices at room temperature to that of the Xe source. Fast carrier relaxation<sup>17,18</sup> within the wells should compensate for slight changes in excitation energy distribution between the two optical sources.

Figure 1 shows the results of an equilibrium energy band simulation for samples A, B, and C by the SiLENSe version 5.2 software.<sup>19</sup> The assumed level of unintentional n-type doping for these simulations was estimated at  $5 \times 10^{16} \text{ cm}^{-3}$  for the InGa<sub>N</sub> quantum wells and  $2 \times 10^{16} \text{ cm}^{-3}$  for the GaN layers, as this is approximately the level seen for oxygen doping (a known shallow donor in GaN<sup>20</sup>) in these materials. As can be seen in the full structure diagrams on the left of Fig. 1, the UID MQW regions are expected to be fully depleted at zero bias. This conclusion matches well with capacitance-voltage (C-V) measurements performed on C-V structures located on the same wafer as the solar cells presented. On the right of Fig. 1, a difference in QW field strength of  $\sim 0.4 \text{ MV/}$

cm between samples A and C is apparent. The origin of this behavior is primarily due to the constant potential drop of the built-in potential ( $V_{\text{BI-GaN}} \sim 3.3 \text{ V}$ ) being distributed over a larger distance in the thicker structures. The field in a well ( $F_{\text{QW}}$ ) is given as a sum of the built-in field ( $F_{\text{BI}}$ ), the polarization field ( $F_{\text{Pol}}$ ), and the applied field ( $F_{\text{App}}$ ) as follows:

$$F_{\text{QW}} = F_{\text{BI}} + F_{\text{Pol}} - F_{\text{App}}. \quad (1)$$

In the case of a fully-depleted p-i-n diode with heavily doped end-regions and a p-type surface in the (0001) orientation, Eq. (1) can be approximated by assuming all the field is dropped across the i-region

$$F_{\text{QW}} \cong \frac{V_{\text{BI}}}{t_i} - \frac{\sigma_{\text{pol}}}{\epsilon} - \frac{V_{\text{App}}}{t_i}, \quad (2)$$

where  $t_i$  is the thickness of the i-region,  $\sigma_{\text{pol}}$  is the polarization sheet charge density at the heterointerfaces,  $\epsilon$  is the electric permittivity of the semiconductor, and  $V_{\text{BI}}$  and  $V_{\text{App}}$  are the built-in and applied potentials, respectively. Because  $\sigma_{\text{pol}}$  is a material constant depending only on the composition and crystal orientation (Ref. 21)—and not any dimension of the device—so, too, is the field produced by the charge. By varying only the barrier thicknesses and applied bias, we are modifying only the  $F_{\text{BI}}$  and  $F_{\text{App}}$  terms.

Once the origin of internal fields is understood, application of bias during measurement provides insight into the device operation. In Fig. 2, the external quantum efficiency of samples A, B, and C is shown under several biased conditions. At zero bias, the EQE was strongly dependent on barrier thickness, with the peak varying from  $\sim 6\%$  for the 9.7 nm barrier sample to  $\sim 27\%$  for the thin barrier case. By reverse biasing the structures to a uniform  $-5 \text{ V}$ , all three cases reach the same peak EQE of  $\sim 31.5\%$ . Because of the thin ( $\sim 37 \text{ nm}$  total InGa<sub>N</sub>) absorber structure and significant ( $\sim 18\%$ ) Fresnel surface reflection losses, it is estimated that this peak EQE corresponds to a peak internal quantum efficiency (IQE) approaching 100% for this bias. By setting Eq. (2) equal to zero and solving for  $V_{\text{App}}$ , the flat-band

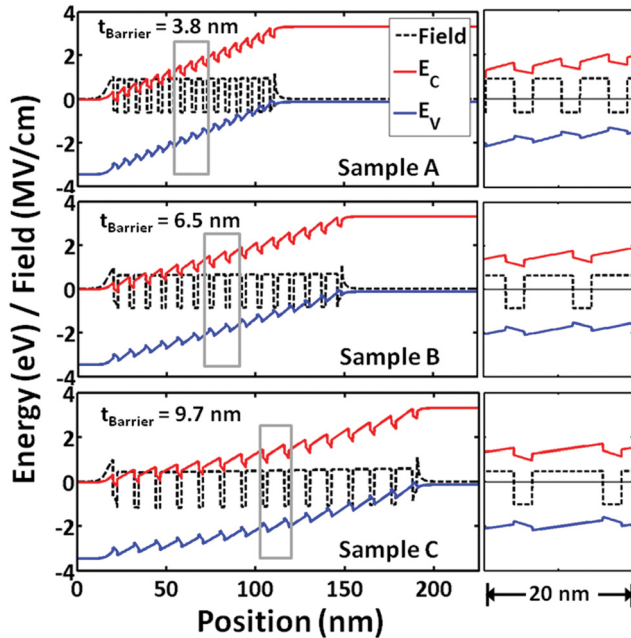


FIG. 1. (left) Simulated equilibrium band diagrams (0 applied bias) coplotted with the field strength as a function of position for samples A, B, and C. (right) Enlarged views of center 20 nm (boxed) of each structure for clarity.

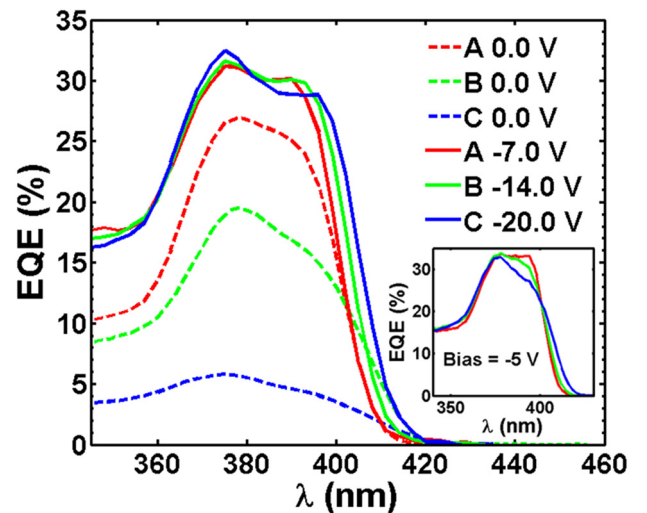


FIG. 2. External quantum efficiency for samples A, B, and C plotted at 0 applied bias (dotted curve), reverse bias corresponding to calculated flat-band quantum wells (solid curve), and a uniform reverse bias of  $-5 \text{ V}$  (inset).

conditions for wells in the different structures can be found. These biases are approximately  $-7$ ,  $-14$ , and  $-20$  V for samples A, B, and C, respectively. EQE curves for these bias conditions are also shown in Fig. 2. In QW-flat-band conditions, the EQE spectra for the three samples become nearly equivalent, with some slight spectral shift likely due to run-to-run growth variation.

The dependence of photocurrent on barrier thickness, temperature, and bias is similarly apparent. Figure 3 demonstrates that a sufficiently large reverse bias can increase the collection efficiency to near 100% for carriers photogenerated in all three structures. The same field dependence indicated by the spectrally resolved measurements is also present in the room-temperature measurements of Fig. 3, as all three of the samples tend towards photocurrent saturation at the same density of  $\sim 0.6$  mA/cm<sup>2</sup> at a reverse bias of  $-5$  V. From temperature dependent reverse biased EQE measurements (flat-well condition), the absorption edge was observed to shift from 414 nm (2.99 eV) to 420 nm (2.95 eV) while heating from 296 to 393 K. This reduction in bandgap energy at elevated temperature accounts for the increase in the saturated photocurrent at  $-5$  V, as the QW layers are then able to absorb additional photons. Upon heating from 296 to 393 K the illuminated J-V curves for sample C exhibited a significant increase in fill factor (FF) (28%–39%) and short-circuit current density ( $J_{SC}$ ) (0.14–0.41 mA/cm<sup>2</sup>), while sample A remains relatively unaffected, with an increase in FF from 66% to 69% and  $J_{SC}$  from 0.54 to 0.58 mA/cm<sup>2</sup>. The cryogenic measurements extend the range over which this behavior was observed, where sample C displayed a marked drop in FF and  $J_{SC}$  at low temperature in comparison to high temperature, while sample A again remained unaffected. These data indicate a strongly temperature dependent mechanism

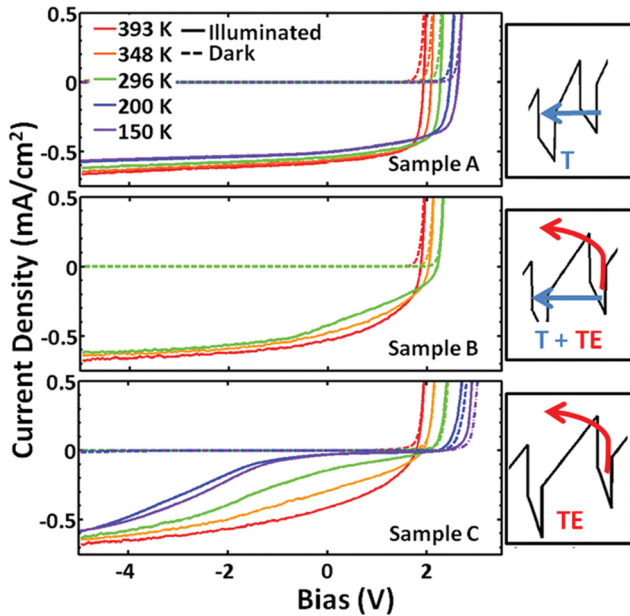


FIG. 3. (left) Current density vs. bias for samples A, and C having 3.8, and 9.7 nm barriers, respectively, as a function of temperature from 150 to 393 K with and without 1-sun intensity illumination. Data for sample B, with 6.5 nm barriers, is also shown from 296 to 393 K. (right) Schematics for relevant escape mechanisms for each sample: T=tunneling and TE=thermionic emission.

dominates in the sample with thick barriers until large reverse bias, while a temperature *independent* mechanism dominates for the thin barrier sample.

To understand this change in temperature dependence amongst the samples with different barrier thicknesses, it is useful to consider all of the processes by which photogenerated carriers in a MQW p-i-n photodiode or solar cell are either lost or, alternatively, contribute to the photocurrent. A formulation in terms of carrier lifetimes ( $\tau$ ) as a competition between recombination and escape mechanisms is as follows:<sup>22</sup>

$$\frac{1}{\tau} = \frac{1}{\tau_R} + \frac{1}{\tau_{NR}} + \frac{1}{\tau_T} + \frac{1}{\tau_{TE}}, \quad (3)$$

where  $\tau_{NR}$  and  $\tau_R$  represent the lifetimes for non-radiative and radiative recombination, and  $\tau_T$  and  $\tau_{TE}$  represent lifetimes for tunneling and thermionic emission. The loss mechanisms for photocarriers produced in a QW photodetector or solar cell are both non-radiative and radiative recombination. Little “photon recycling” is possible in these InGaN MQW structures, because radiative emission from the QWs occurs at long (QCSE red-shifted) wavelengths, where the absorption is negligible. The mechanisms that allow a carrier to escape the QW and potentially contribute to the photocurrent at the contacts are tunneling through the barrier and thermionic emission over the barrier. The thermionic emission mechanism for carrier emission over a single barrier primarily depends exponentially on temperature through the carrier population energy distribution near the top of the barrier.<sup>23</sup> However, a field-dependence of the thermionic emission mechanism should also appear through field-assisted barrier lowering.<sup>24</sup> A field-assisted (Fowler-Nordheim type) tunneling mechanism through thin barriers should remain temperature independent but exhibit significant field-dependence through barrier-lowering and narrowing, as the tunneling rate should show nearly exponential increase with decreasing effective barrier height and width.

To gauge the relative significance of the escape mechanisms under bias, the potential profile and quantum-confined eigenstates of the three structures were simulated using a custom self-consistent Schrödinger-Poisson drift-diffusion solver.<sup>25</sup> After calculating these parameters of the structure with this method,  $\tau_T$  was estimated<sup>26</sup> by calculating the product of an attempt rate as a function of carrier velocity ( $\frac{v}{L_w}$ ) and a tunneling probability from a given QW state energy ( $T(E_n)$ ) through a WKB-approximation<sup>27</sup>

$$\frac{1}{\tau_T} = \frac{v}{L_w} T(E_n) = \frac{n\pi\hbar}{2L_w^2 m^*} \exp \int_0^{L_b} -2\sqrt{\frac{2m^*(E_{c,v}(x) - E_n)}{\hbar^2}} dx. \quad (4)$$

Additionally,  $\tau_{TE}$  was calculated using the same profiles and by identifying the maximum potential in the applicable barrier ( $E_{c,vmax}$ )

$$\frac{1}{\tau_{TE}} = \left( \frac{k_B T}{2\pi m^* L_w^2} \right)^{1/2} \exp \left( -\frac{E_{c,vmax} - E_n}{k_B T} \right). \quad (5)$$



In both Eqs. (4) and (5),  $k_B$  is Boltzmann's constant,  $T$  is the absolute temperature,  $L_w$  and  $L_b$  are QW and barrier thickness, respectively, while the effective masses ( $m^*$ ) used were  $0.169m_0$  for electrons and  $1.83m_0$  for heavy holes. In both cases, only the ground-state ( $n = 1$ ) was considered, as this is a "worst-case" for carrier escape.

The results of the calculated lifetimes for the three different structures at 300 and 400 K and bias ranging from  $-5$  to  $+3$  V<sub>App</sub> are presented in Fig. 4. As expected, all escape lifetimes show field dependence, decreasing with increasing reverse bias, and the dominance of tunneling over thermionic emission for negative bias is apparent. The smaller electron effective mass promotes faster escape for electrons than for holes for all conditions. The relative importance of thermionic emission vs. tunneling for a given bias shifts when the calculation is performed instead at 400 K, with  $\tau_{TE}$  decreasing for increased temperature and  $\tau_T$  remaining essentially constant. For the thinnest barriers (sample A), tunneling remains dominant at all temperatures and biases, while thermionic emission becomes comparable (sample B) or dominant (sample C) for the 400 K case near and above zero bias.

By comparing the calculated results of Fig. 4 to the empirical results of Fig. 3, some conclusions may be drawn about carrier transport in these devices. From Fig. 3, current saturation corresponding to maximized IQE did not occur for all samples until significant ( $\sim -5$  V) reverse bias was applied. According to the results in Fig. 4, the dominant mechanism at this bias for all samples was tunneling. The trend of decreasing FF for samples B and C follow from their decreased tunneling efficiency. This tunneling deficiency is partially compensated at elevated temperature with an

increased TE efficiency resulting in increased FF. For all cases, it is likely that once carriers are able to extract with significant probability, they will emit to continuum states and drift until fully extracted from the MQW region or are recaptured in a QW where they may attempt extraction again, similar to Larson's "high-field" regime.<sup>26</sup>

In conclusion, carrier transport mechanisms in InGaN MQW solar cells were investigated by varying barrier thicknesses in the MQW structure. Comparing calculated thermionic emission and tunneling lifetimes with temperature-dependent illuminated J-V measurements indicated a tunneling-dominated transport process, with thermionic emission gaining dominance only for thick barriers and high temperatures.

The authors would like to thank C. Weisbuch and D. Cohen for helpful discussions. This work was supported by the DARPA High Performance InGaN-Based Solar Cells Program (Grant No. HR0011-10-1-0049), the California Advanced Solar Technologies Institute (CAST) (Grant No. 143188), and the Solid State Lighting and Energy Center (SSLEC). R.M.F. was partially supported by the Center for Energy Efficient Materials (CEEM) at UCSB, an Energy Frontier Research Center funded by the U.S. DOE (Grant No. DE-SC0001009). Y.-R.W. was partially funded by the National Science Council in Taiwan under Grant Nos. NSC-100-2918-I-002-052 and NSC 99-2221-E-002-058-MY3. A portion of this work was done in the UCSB nanofabrication facility, part of the NSF NNIN network (Grant No. ECS-0335765), as well as the UCSB MRL, which is supported by the NSF MRSEC program (Grant No. DMR11-21053).

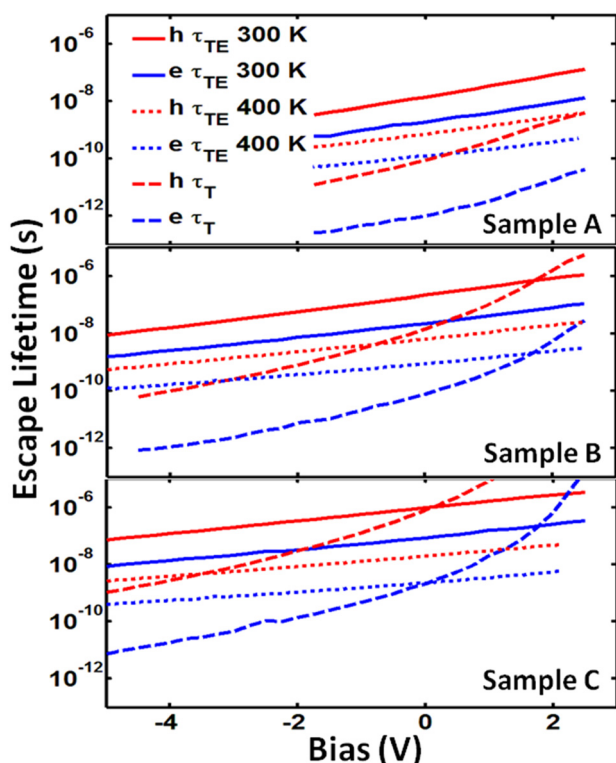


FIG. 4. Calculated lifetimes for thermionic emission (TE) at 300 K and 400 K and tunneling (T) at 300 K for electrons (e) and holes (h) from the lowest energy bound states of the quantum wells in the three structures.

- <sup>1</sup>S. P. Bremner, M. Y. Levy, and C. B. Honsberg, *Prog. Photovoltaics* **16**, 225 (2008).
- <sup>2</sup>N. G. Toledo, D. J. Friedman, R. M. Farrell, E. E. Perl, C.-T. Lin, J. E. Bowers, J. S. Speck, and U. K. Mishra, *J. Appl. Phys.* **111**, 054503 (2012).
- <sup>3</sup>N. G. Toledo and U. K. Mishra, *J. Appl. Phys.* **111**, 114505 (2012).
- <sup>4</sup>R. Dahal, B. Pantha, J. Li, J. Y. Lin, and H. X. Jiang, *Appl. Phys. Lett.* **94**, 063505 (2009).
- <sup>5</sup>R. M. Farrell, C. J. Neufeld, S. C. Cruz, J. R. Lang, M. Iza, S. Keller, S. Nakamura, S. P. DenBaars, U. K. Mishra, and J. S. Speck, *Appl. Phys. Lett.* **98**, 201107 (2011).
- <sup>6</sup>C. J. Neufeld, N. G. Toledo, S. C. Cruz, M. Iza, S. P. DenBaars, and U. K. Mishra, *Appl. Phys. Lett.* **93**, 143502 (2008).
- <sup>7</sup>X. Chen, K. D. Matthews, D. Hao, W. J. Schaff, and L. F. Eastman, *Phys. Status Solidi A* **205**, 1103 (2008).
- <sup>8</sup>Z. Q. Li, M. Lestrade, Y. G. Xiao, and S. Li, *Phys. Status Solidi A* **208**(4), 928 (2011).
- <sup>9</sup>J. J. Wierer, Jr., A. J. Fischer, and D. D. Koleske, *Appl. Phys. Lett.* **96**, 051107 (2010).
- <sup>10</sup>C. J. Neufeld, S. C. Cruz, R. M. Farrell, M. Iza, J. R. Lang, S. Keller, S. Nakamura, S. P. DenBaars, J. S. Speck, and U. K. Mishra, *Appl. Phys. Lett.* **98**, 243507 (2011).
- <sup>11</sup>J. J. Wierer, Jr., D. D. Koleske, and S. R. Lee, *Appl. Phys. Lett.* **100**, 111119 (2012).
- <sup>12</sup>D. A. B. Miller, D. S. Chemla, T. C. Damen, A. C. Gossard, W. Wiegmann, T. H. Wood, and C. A. Burrus, *Phys. Rev. Lett.* **53**, 2173 (1984).
- <sup>13</sup>C. A. Humi, O. Bierwagon, J. R. Lang, B. M. McSkimming, C. S. Gallinat, E. C. Young, D. A. Browne, U. K. Mishra, and J. S. Speck, *Appl. Phys. Lett.* **97**, 222113 (2010).
- <sup>14</sup>A. Dussaigne, B. Damilano, J. Brault, J. Massies, E. Feltrin, and N. Grandjean, *J. Appl. Phys.* **103**, 013110 (2008).
- <sup>15</sup>J. R. Lang and J. S. Speck, *J. Cryst. Growth* **346**, 50 (2012).
- <sup>16</sup>J. R. Lang, C. J. Neufeld, C. A. Humi, S. C. Cruz, E. Matioli, U. K. Mishra, and J. S. Speck, *Appl. Phys. Lett.* **98**, 131115 (2011).

- <sup>17</sup>H.-C. Wang, S.-C. Lin, Y.-C. Lu, Y.-C. Cheng, C. C. Yang, and K.-J. Ma, [Appl. Phys. Lett.](#) **85**, 1371 (2004).
- <sup>18</sup>H. Ye, G. W. Wicks, and P. M. Fauchet, [Appl. Phys. Lett.](#) **74**, 711 (1999).
- <sup>19</sup>V. F. Mymrin, K. A. Bulashevich, N. I. Podolskaya, I. A. Zhmakin, S. Yu. Karpov, and Yu. N. Makarov, [Phys. Status Solidi C](#) **2**, 2928 (2005).
- <sup>20</sup>C. G. Van de Walle and J. Neugebauer, [J. Appl. Phys.](#) **95**, 3851 (2004).
- <sup>21</sup>A. E. Romanov, T. J. Baker, S. Nakamura, and J. S. Speck, [J. Appl. Phys.](#) **100**, 023522 (2006).
- <sup>22</sup>A. M. Fox, D. A. B. Miller, G. Livescu, J. E. Cunningham, and W. Y. Jan, [IEEE J. Quantum Electron.](#) **27**, 2281 (1991).
- <sup>23</sup>S. M. Sze and K. K. Ng, *Physics of Semiconductor Devices*, 3rd ed. (Wiley, New York, 2007).
- <sup>24</sup>H. Schneider and K. v. Klitzing, [Phys. Rev. B](#) **38**, 6160 (1988).
- <sup>25</sup>Y.-R. Wu, M. Singh, and J. Singh, [J. Appl. Phys.](#) **94**, 5826 (2003).
- <sup>26</sup>A. Larsson, P. A. Andrekson, S. T. Eng, and A. Yariv, [IEEE J. Quantum Electron.](#) **24**, 787 (1988).
- <sup>27</sup>M. Singh and J. Singh, [J. Appl. Phys.](#) **91**, 2989 (2002).